WIND-DRIVEN INERTIAL WAVES OBSERVED DURING PHASE III OF GATE

R. H. Käse and D. J. Olbers

Institut für Meereskunde, Kiel, Federal Republic of Germany

ABSTRACT

Current and wind stress time series obtained from the F1-mooring are analysed with the aim of examining linear correspondences and testing the adequacy of linear coupling models at near-inertial frequencies. Significant linear correlations are found in the data set which are consistent with a linear wind-driven model of the current system. The current in the mixed layer can be described by inertial oscillations directly forced by the local wind stress. A wind-driven simulation model of the mixed layer currents yields an energy input of $3 \cdot 10^{-3}$ W/m^2. The current in the thermocline can be described by a linear internal wave field of downward propagating wave groups driven via Ekman suction by the wind stress field. Internal waves are generated at a rate of 10^{-3} W/m^{-2}, consistently estimated from both kinematic and dynamic considerations.

INTRODUCTION

Velocity oscillations with an inertial period have been observed in the ocean and large lakes at all latitudes and depths. In general, an 'inertial peak' dominates the spectra of horizontal currents in the frequency band of internal waves. Since these motions make a major contribution to the kinetic energy in the mixed layer as well as in the stratified water below considerable effort has been spent in recent years to establish their basic characteristics and to study their generation and decay. There is agreement among oceanographers about the most prominent characteristics, namely the clockwise rotation (in the northern hemisphere) of the horizontal current vector with time, a dominant frequency which is slightly higher than the local inertial frequency (e.g. Day and Webster, 1965; Gonella, 1971; Kundu, 1976), coherence scales of a few tens of metres for vertical and a few tens of kilometres for horizontal separations (e.g. Webster, 1968; Schott, 1971), upward propagation of phase and clockwise turning of the velocity vector with increasing depth (e.g. Kundu, 1976; Leaman, 1976; Perkins and Van Leer, 1977). These features can also be found in the kinematical structure of near-inertial internal waves in the IWEX spectrum (Müller and others, 1978).

Except for intermittent occurrence of the oscillations in space and time (e.g. Webster, 1968) and some relation of near surface currents to the wind, no clear signatures have been observed which point towards a particular generation

process. Hence, a variety of partly controversial concepts have been put forward
to explain the generation of near-inertial oscillations. It is generally agreed
that the wind is the driving force for inertial motions in the mixed layer. A
linear correspondence between currents and the local wind as substantiated e.g.
by Gonella (1971, 1972) could be exploited to construct simple linear forcing
models as the one of Pollard and Millard (1970) which successfully simulates
near-surface currents (e.g. Kundu, 1976; McPhee, 1978, Daddio and others, 1978).
However, no clear relation has been detected between the internal wave motion
below the mixed layer and the surface forcing function, in particular the wind
stress (e.g. Webster, 1968). There are models which do not directly involve the
wind, such as Hasselmann's (1970) model in which inertial oscillations are
driven by the Stokes drift associated with surface waves. Stern (1977) considered
interaction with the mean current in the mixed layer as driving mechanism. Even
non-linear generation is conceivable. Thus Olbers (1976) suggested that the
inertial peak of mid-ocean spectra is a consequence of balancing the quasi-
equilibrium spectral shape by non-linear interaction within the internal wave
field. Evidence for nonlinearity in the wind-current momentum transfer has been
found by Yao and others (1977) in data gathered on the Oregon shelf.

The lack of coherence across the base of the mixed layer, however, does not
necessarily demand non-linear models. If a description of the currents in the
thermocline as vertically propagating internal waves is adequate, then upward
propagating phase implies a downward flux of wave energy. Hence generation at
the surface seems to be likely. The lack of coherence may then be explained by
the almost horizontal characteristics of near-inertial waves. The energy has
been transferred into the ocean far away from the point of observation in the
thermocline and the local coherence between currents and wind may be in-
significant.

In the GATE field programme an internal wave experiment was performed which was
specifically designed to study the kinematical and dynamical characteristics of
internal waves in the upper ocean. A description of the experiment and data is
presented in this volume (Käse and Siedler, 1979). In the present work a subset
of the data is used to investigate the coupling between the wind stress and
currents in and below the mixed layer. By detrending the time series and
applying a low-pass filter a broad band around the inertial frequency is
retained. With these filtered time series the relevance of linear forcing is
demonstrated by studying time-lagged correlations of wind stress and currents
at several depths. Since the resolution of our experiment is too low to test the
relevance of different linear coupling models we restrict the analysis to show
linear correspondences and give some interpretation in terms of the simplest
linear models.

In part 3 we show by correlation methods and simulation of the correlation
pattern by a linear model that the momentum transfer from wind to the mixed
layer is basically linear. Part 4 deals with some kinematic characteristics of
the internal wave field in the upper thermocline. In particular we analyse the
direction of the vertical energy flux. It is found that energy propagates down-
ward at a rate which is in rough agreement with previous estimates. Linear
correspondences between the motions in the thermocline, the mixed layer current,
and the wind stress are revealed in part 5. Correlations between these fields
are obvious but are only marginally significant, as may be expected in view of
non-stationary conditions and possible contamination of the current by motions
not related to the wind. As noted above, in a linear model even the wind-driven
part of the motion in the thermocline is not directly related to the local wind
stress. The appearance of a local correlation thus must be attributed to a large
horizontal correlation scale of the wind stress field at periods of a few days
which was observed in the GATE area (Reed and others, 1977). Further evidence

for wind-driven waves is discussed in part 6. In particular the energetics of the coupling and relations between the correlation pattern of wind stress and that one of the wave field are examined.

DATA SET

The data used in this work are part of the internal wave experiment performed during the third phase of the GATE field programme in 1974 near the equator. The current meter array was supported by the H-shaped mooring F1 launched at $8^{\circ}44.76'$ N, $23^{\circ}4.24'$ W. It covered horizontal separations from a few metres to about 500 m and vertical separations from a few metres to about 250 m in the upper ocean. About 19 days of current data and 17 days of wind data have been obtained. We have used the wind data and current data from instruments 12, 15, 16 and 17 (VACM) and 18, 19 and 22 (Aanderaa). These have almost purely vertical separations. The average profile of the buoyancy frequency $N(z)$ and profiles of the mean current components are displayed in Fig. 1. The mooring was located in the North Equatorial Counter Current which has an almost eastward direction. Wind stress was computed from $\tau = C_D \rho_a u|u|$ where $C_D = 1.3 \times 10^{-3}$, $\rho_a = 1.22 \times 10^{-3} g$ cm^{-3} and u is the wind velocity logarithmically extrapolated to a standard height of 10 m.
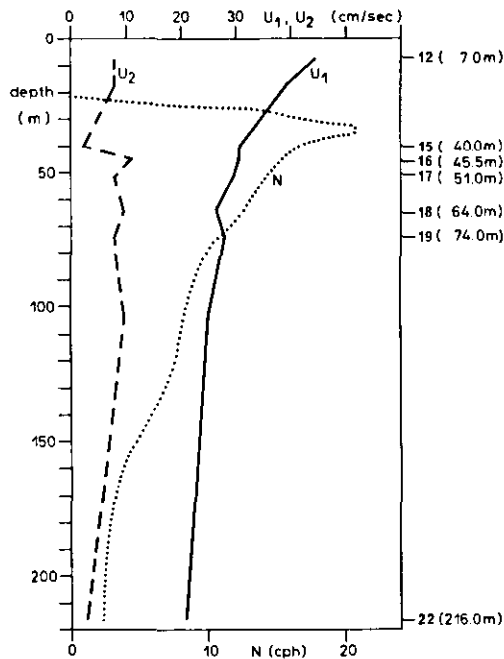

Fig. 1. Profiles of buoyancy frequency $N(z)$ and mean current
components $U_1(z)$ (east) and $U_2(z)$ (north) at the F1-site.
Instrument positions are indicated.
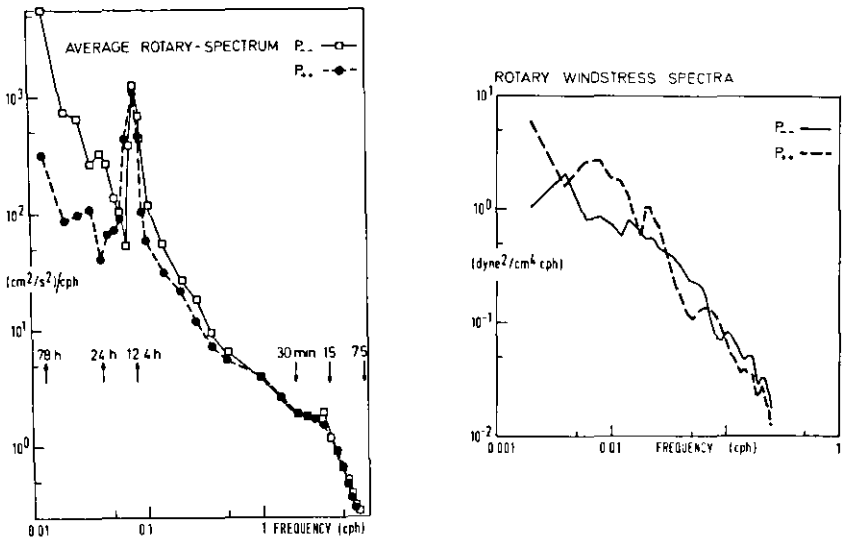
Fig. 2. Rotary spectra of currents (average of 5 horizontally spaced
        instruments at 56 m depth from F1) and wind stress (data
        from E3).

The distribution of energy in the frequency domain is demonstrated in the plots
of rotary current and wind stress spectra in Fig. 2. Note the separation of the
current spectra by two spectral gaps into three parts: a low-frequency part
around the local inertial frequency $f = 0.0128$ cph (period 78.16 h), a tidal
peak, and a high-frequency part above the buoyancy frequency of the water column
beneath the upper thermocline (about 2 cph). This latter part is discussed by
Käse and Siedler (1979). In agreement with linear internal wave theory (e.g.
Müller and others, 1978) the main contribution of the low-frequency energy is
contained in the clockwise rotating part of the motion. The spectra of wind
stress show a concentration of energy between 2 and 4 days with a slight
dominance of the counterclockwise rotating component.

For the analysis described in this paper the time series were converted to
hourly values and linear trends were removed by a least-squares method. Then
a low-pass filter (Lanczos taper with 40 h band limit) was applied which
eliminates high frequencies and retains a broad inertial band. The total length
of the records was recovered by adding zeroes before filtering. Particular care
was taken so that the filtering procedure conserved the relative phases between
the time series because this is an essential requirement in our correlation

analysis. The combination of detrending and low-pass filtering was chosen since the relatively short duration of the experiment prohibited isolation of the inertial frequency by a band-pass filter.
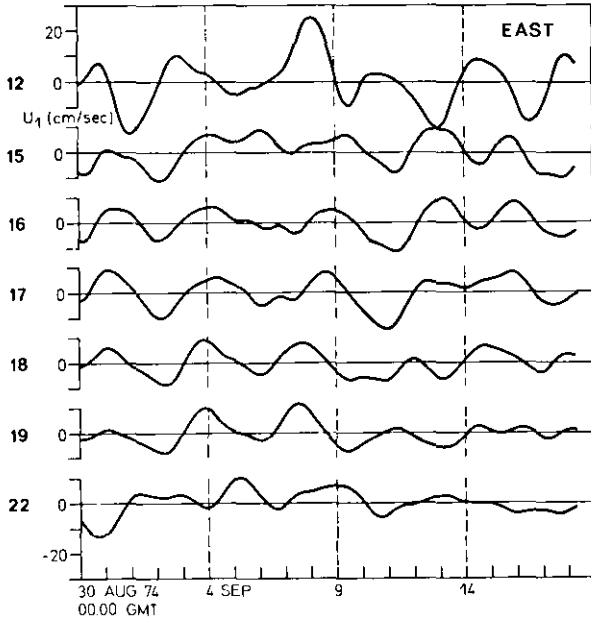

Fig. 3. Eastward component of filtered current at all depths.

The filtered current time series are displayed in Fig. 3, starting on 30 August 0 hours GMT with 464 hourly values. Only east components are shown, the north components have a similar appearance except for slight differences in the r.m.s. values (see Table 1). The dominant period of the currents is about 3 days which is roughly the local inertial period. Except for an event of higher period in the first half of the experiment the wind stress variations show a similar time scale.

TABLE 1 Depths and r.m.s. values of filtered time series of wind stress and current components

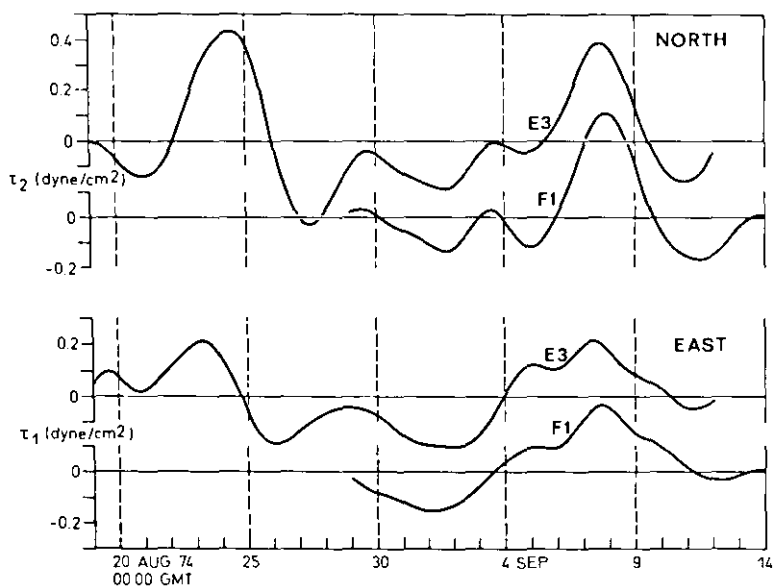| Instrument | Depth (m) | r.m.s. values | |
		East	North
Wind stress	- 10.0	0.18 dyn/cm^2	0.24 dyn/cm^2
12	7.0	10.2 cm/sec	9.0 cm/sec
15	40.0	5.4	7.1
16	45.5	5.0	5.7
17	51.0	5.9	6.5
18	64.0	4.9	5.1
19	74.0	4.5	4.3
22	216.0	4.0	5.3

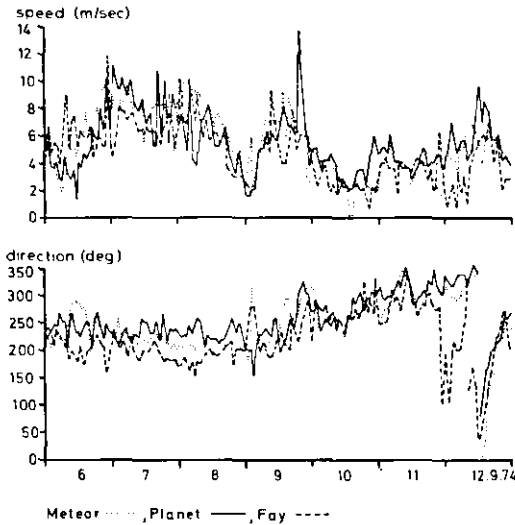Fig. 4. Filtered wind stress components at F1 and E3.

Fig. 5. Wind speed and direction in the C-scale triangle from
research vessels Meteor, Planet and Fay (with kind
permission of E. Augstein).

The magnitude of the horizontal coherence scale of the wind field at these
periods is demonstrated in Figs. 4 and 5 showing wind stress and wind time
series at different stations in the GATE region. Mooring E3 is located about
30 km southeast of F1. The wind stress is completely coherent over this
distance. The coherence scale of periods of some days is obviously much larger
as can be seen in the wind time series of the three ships Planet, Meteor and Fay
which are about 100 km apart (Fig. 5).

For the purpose of detecting linear correspondences in the data auto- and cross-
correlation functions have been computed. Autocorrelations ρ_x (ℓ) of the time
series X_s are estimated by

$$r_x \; (\ell) \; = \; \sum_1^{n-\ell} X_s X_{s-\ell} \; / \; \sum_1^{n} X_s^2 \qquad\qquad (1)$$

where n is the number of data points. Under very general conditions (e.g. Hannan, 1960) $n^{1/2} \{r_x(\ell) - \rho_x(\ell)\}$ is asymptotically normal with zero mean and variance

$$\text{Var } \{r_x(\ell)\} \sim \frac{1}{n} \sum_{-\infty}^{+\infty} \rho_x^2(s) \tag{2}$$

We do not know the true autocorrelation but have a rough impression of the shape of the spectrum $F_x(\omega)$ of X_s. Thus the variance is conveniently estimated from

$$\text{Var } \{r_x(\ell)\} \sim \frac{1}{T} \int_{-\infty}^{+\infty} F_x^2(\omega) \, d\omega \, / \, (\int_{-\infty}^{+\infty} F_x(\omega) \, d\omega)^2 = \frac{1}{2 \, TB_x} \tag{3}$$

where B_x is the spectral band width of $F_x(\omega)$ and T the record length.

Cross-correlations $\rho_{xy}(\ell)$ are estimated in analogy to (1). Confidence limits for zero true correlation $(\rho_{xy} \equiv 0)$ follow from the t-test stating that $(\upsilon-2)^{1/2} \, r_{xy} \cdot (1 - r_{xy})^{-1/2}$ has a $t_{\upsilon-2}$ distribution. The degrees of freedom, υ, are less than the number of data points because of dependence in the time series. Under the hypothesis $\rho_{xy} \equiv 0$ the variance of the estimator asymptotically becomes

$$\text{Var } \{r_{xy}(\ell)\} \sim \frac{1}{T} \int_{-\infty}^{+\infty} F_x(\omega) \, F_y(\omega) \, d\omega / (\int_{-\infty}^{+\infty} F_x(\omega) \, d\omega \cdot \int_{-\infty}^{+\infty} F_y(\omega) \, d\omega) \tag{4}$$

which is bounded by $(2T(B_x B_y)^{1/2})^{-1}$. Thus, approximately

$$\upsilon \simeq 1/\text{Var } \{r_{xy}\} \geqslant 2T(B_x B_y)^{1/2}. \tag{5}$$

The value of υ measures the effective number of independent data points in the time series. In our case $T \, (B_x B_y)^{1/2} = O(10)$. The figures of cross-correlations include the 90 % confidence limits for $\upsilon = 20$.

Cross-correlation functions are presented and discussed in the following chapters. Autocorrelation functions of the wind stress and currents at some depths are displayed in Fig. 6. The dominant period in current auto-correlations is about the inertial period. There is a slight difference in the periods of east and north component in the mixed layer (instrument 12) and the upper thermocline (instrument 16 and 17) which disappears with increasing depth (instrument 18 and those below). An explanation of this feature is given in part 4. The autocorrelations of the wind stress reveal similar time scales as those of the currents but behave more complexly due to the absence of one dominant peak in the spectra.
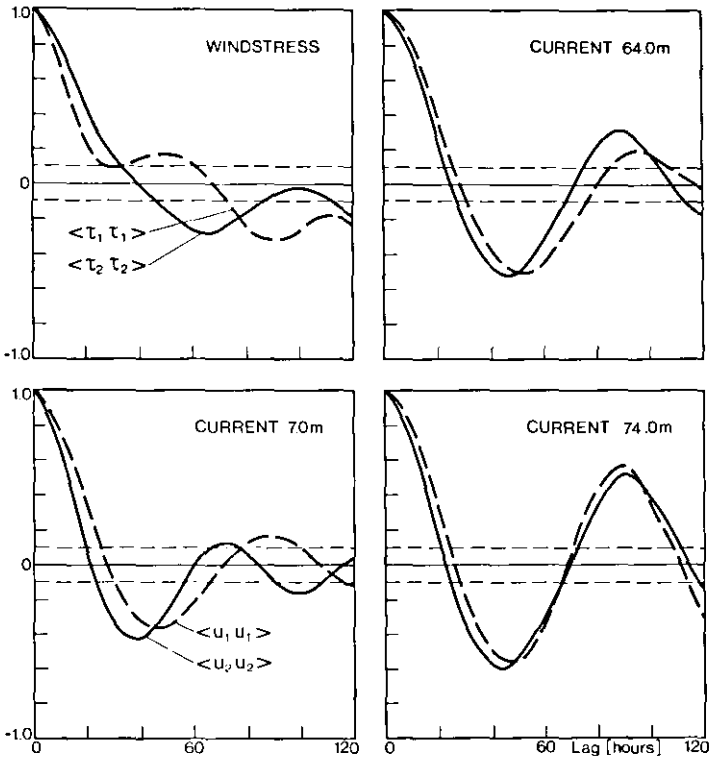
Fig. 6. Autocorrelation functions of wind stress and currents from
7 m, 51 m and 74 m depth. Dashed lines indicate two
standard deviations.

WIND-FORCING OF THE MIXED LAYER CURRENTS

It is generally accepted that inertial motions in the mixed layer are excited
directly by the wind stress at the surface. Satisfactory progress has been made
with simple linear models like the one of Pollard and Millard (1970). In this
model the wind stress is treated as constant body force in a mixed layer of
constant depth d. Dissipation and radiation of energy into the thermocline is
modelled by a linear damping term. Thus

$$G : = \partial_t u_\alpha - \epsilon_{\alpha\beta} \, f u_\beta = \frac{1}{\rho \cdot d} \tau_\alpha - r u_\alpha \quad (\alpha = 1,2) \qquad (6)$$

An alternative but essentially equivalent way of coupling is to transmit the
surface stress into the interior via turbulent shear stress parameterized by
an eddy viscosity. This Ekman-type model has some points in its favour since it
allows for vertical shear. Models of this kind are able to reproduce observed
currents but fail, of course, if the inherent assumption of local forcing is not
adequate as in the case of advection and non-linearities. The model (6) was
successfully applied to the F1 and E3 mixed layer currents by Redell (1979) with
r^{-1} of about 300 h. Here we discard the simulation of individual events and
attempt to verify linear coupling in the average by studying correlation
functions.

Some correlations between wind stress and mixed layer current are included in
Fig. 8 below (upper panels). Around zero lag some significant estimates are
found at the 90 % confidence level. A much clearer picture (Fig. 7) of the
coupling is gained by correlating the time series $G_\alpha(t)$ with the stress
components $\tau_\alpha(t)$. This procedure eliminates free inertial oscillations but
retains the forced part of the motion. Positive correlation at zero lag
demonstrates the principle balance (6) of a linear model. A secondary peak in
the correlation of east components ($\alpha = 1$) at lags around 50 h must obviously
be attributed to autocorrelations of τ_1 (see Fig. 6).

The free parameters (such as d and r in (6)) of a linear prediction model may
be determined by correlation methods. This is essentially equivalent to fitting
an auto-regressive process to the data, a method proposed by Mofjeld and Mayer
(1976) to simulate wind-driven currents. A rough estimate of the mixed layer
depth obtained from $<G_\alpha \tau_\alpha> = <\tau^2>/\rho d$ is d = 30 m which favourably agrees with
the observed value. We did not proceed in the direction of detailed model fitting
and prediction. Instead we show that a linear model is able to simulate the
observed correlations. For this purpose an Ekman model

$$G_\alpha = (\mu u'_\alpha)'$$

$$\mu u'_\alpha = \tau_\alpha \text{ at } z = 0 \tag{7}$$

$$u_\alpha = 0 \text{ at } z = -d$$

has been driven by the wind stress at E3 (see Fig. 4) starting about 10 days
before our data. Correlations have been computed for the overlapping time inter-
val. The model is designed for a step-functional form of $\mu(z)$. The evolution in
time is integrated numerically by fast Fourier transformation. The parameters μ
and d were tuned to reproduce the observed r.m.s. velocity at 7 m depth and the
shape of the correlation functions. Observed and computed correlations for μ
= 30 cm^2/sec and d = 30 m are displayed in Figs. 7 and 8. Data and model are
quite similar. There is a slight difference in the correlation level (in the
model u_α and τ_β are less correlated whereas G_α and τ_α are better correlated than
observed) and in the overall appearance at positive lags (i.e. correlations of
the stress with past currents).

Included in Fig. 8 are model correlations at the surface z = 0 which may be
used to compute the energy flux $<\tau_\alpha u_\alpha(0)>$ into the surface layer. In
contrast to greater depths both pairs τ_α and u_α, $\alpha = 1,2$, are in phase at the
surface giving positive contributions to the flux which is estimated as
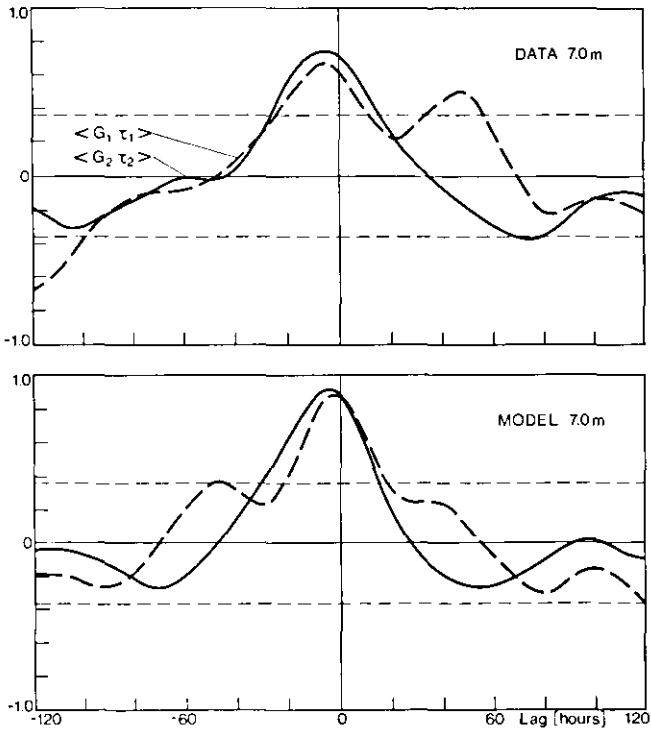3.3 · 10^{-3} W/m^2.

Fig. 7. Cross-correlation functions of $G_\alpha = \partial_t u_\alpha - \varepsilon_{\alpha\beta} f u_\beta$ and τ_α ($\alpha = 1,2$) of data (upper panel) and model (lower panel) at 7 m depth. Dashed lines indicate the 90 % confidence limits.

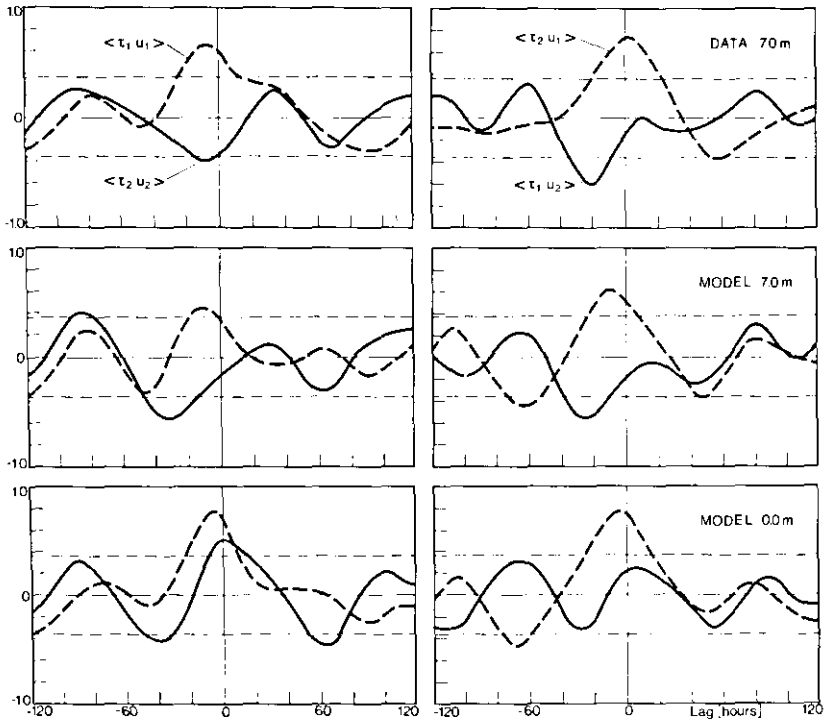Fig. 8. Cross-correlation functions of τ_α and u_β $(\alpha,\beta=1,2)$ of data at 7 m depth (upper panels) and model at 7 m depth (middle panels) and at the surface (lower panels).

THE MOTION IN THE THERMOCLINE

The currents in the thermocline are interpreted as vertically propagating low-frequency internal waves. A detailed test of this assumption in terms of consistency relations, or even a separation of the currents in a wave and a non-wave part (Müller and others, 1978), has not been attempted since the time series are too short for an adequate statistical treatment. Instead, we point out some features in the correlation functions which may be explained by linear internal wave kinematics.

The waves are represented in the WKB approximation. Suppose the field of motion consists of wave packets with frequencies ω and horizontal wave vectors $\underset{\sim}{k} = k \, (\cos\phi, \sin\phi)$. Then, according to WKB

$$
\begin{Bmatrix} u_1 \\ u_2 \\ w \\ p \end{Bmatrix} = \Sigma a_\sigma(\underset{\sim}{k},\omega) \begin{Bmatrix} (-\omega\cos\phi - if\sin\phi)\psi_\sigma'(z)/k \\ (-\omega\sin\phi + if\cos\phi)\psi_\sigma'(z)/k \\ i\omega\,\psi_\sigma(z) \\ -(\omega^2-f^2)\psi_\sigma'(z)/k^2 \end{Bmatrix} e^{i(\underset{\sim}{k}\cdot\underset{\sim}{x}-\omega t)} + c.c.
\tag{8}
$$

where the summation symbol denotes an integral over $\underset{\sim}{k}$ and ω and summation over the sign σ of the vertical wavenumber $\sigma\beta(z)$ where

$$
\beta(z) = k\left(\frac{N^2(z) - \omega^2}{\omega^2 - f^2}\right)^{1/2}
\tag{9}
$$

The vertical eigenfunction is

$$
\psi_\sigma(z) = \psi_\sigma(\underset{\sim}{k},\omega,z) = C(\omega)\left(\frac{k}{\beta}\right)^{1/2}\exp\left\{-i\sigma\int_z^{-d}d\zeta\beta(\zeta)\right\}
\tag{10}
$$

Wave packets with positive σ have an upward vertical phase velocity and downward vertical group velocity. The normalization factor C can be adjusted such that

$$
2\langle a_\sigma(\underset{\sim}{k},\omega)\, a_\sigma^*(\underset{\sim}{k},\omega)\rangle = E_\sigma(\underset{\sim}{k},\omega)
\tag{11}
$$

is the spectral density of the total wave energy (see Müller and others, 1978). The covariance function of current components with purely vertical separation is

$$
R_{\alpha\beta}(z,\zeta,\tau) = \langle u_\alpha(\underset{\sim}{x},z,t)\, u_\beta(\underset{\sim}{x},z-\zeta,t-\tau)\rangle
\tag{12}
$$

$$
= \Sigma\, E_\sigma(\underset{\sim}{k},\omega)\left\{D_{\alpha\beta}\, k^{-2}\psi_\sigma'(z)\left(\psi_\sigma'(z-\zeta)\right)^* e^{-i\omega\tau} + c.c.\right\}
$$

where

$$
\left(D_{\alpha\beta}\right) = \begin{pmatrix} \omega^2\cos^2\phi+f^2\sin^2\phi & \vline & i\omega f + \tfrac{1}{2}(\omega^2-f^2)\sin 2\phi \\ -i\omega f + \tfrac{1}{2}(\omega^2-f^2)\sin 2\phi & \vline & \omega^2\sin^2\phi+f^2\cos^2\phi) \end{pmatrix}
\tag{13}
$$

Approximately, the covariance function is a weighted Fourier transform of the spectrum with respect to frequency ω (strictly true for ζ = 0) and wavenumber k. If E_σ (k,ω) represents a narrow band process $R_{\alpha\beta}$ will show an oscillating behaviour. In the observed correlation functions (see Figs. 6, 9 and 10) this is evident in the dependence on the time lag τ but not in the dependence on the separation lag ζ. In all correlation functions an overall degradation of the correlation amplitudes with increasing lags τ and ζ is visible, which is due to non-vanishing band widths of the spectrum.
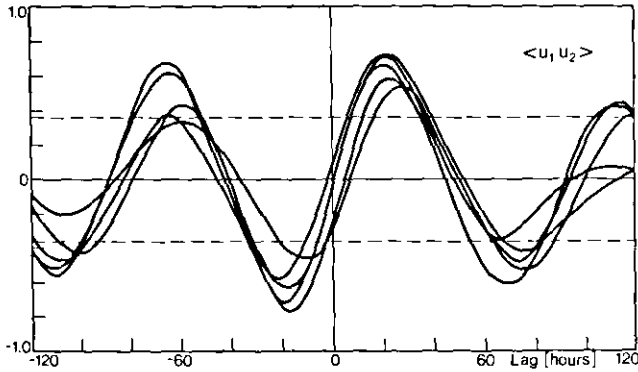

Fig. 9. Cross-correlation functions of u_1 and u_2 at the same
position for the five instruments below the mixed layer.

Figs. 6 and 9 display some correlations of the current components at the same position (i.e. ζ = 0). When interpreted in terms of the internal wave model the difference in the periods of the current autocorrelation functions necessarily requires a horizontally anisotropic energy spectrum. Since the period of R_{11} is longer than that in R_{22} the weighting of the spectrum by the function D_{22} must result in a shift to higher frequencies as compared to the weighting by D_{11}. This is the case if there is a preferred meridional direction in the wave field. At greater depths this anisotropy seems to vanish, as is illustrated by the autocorrelations of the instrument at 74 m depth. An explanation of this feature as an adjustment of the wave field in the upper thermocline (which is anisotropic because of the proximity of the generation region) to a more isotropic wave field in the deep ocean by nonlinear wave interactions is speculative but not inconsistent with further results derived in the following.

For near-inertial waves the current components u_1 and u_2 at a fixed position are almost π/2 out of phase. The wave model (12) additionally implies that R_{12} behaves as sin ωτ around zero lag. This signature is clearly shown in the observed cross-correlations (Fig. 9).
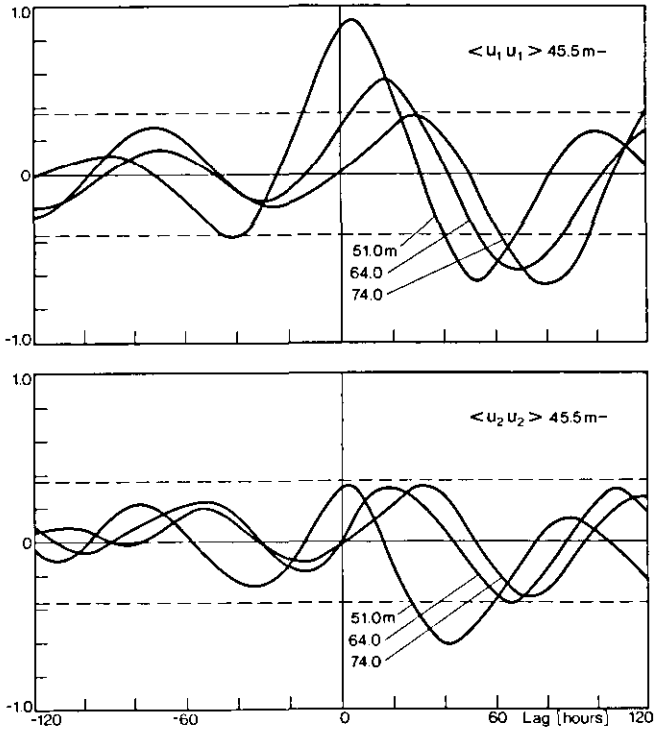
Fig. 10. Cross-correlation functions of u_α at 45.5 m depth with u_α at 51.0 m, 64.0 m and 74.0 m depth, upper panel: east components ($\alpha = 1$), lower panel: north components ($\alpha = 2$).

Some cross-correlations of current components at different depths are shown in
Fig. 10. The pattern of the correlations appear to be similar except for a phase
shift towards positive time lags with increasing separation (i.e. the deeper
instrument leads the upper in phase). These phase shifts allow some conclusions
about the vertical symmetry of the wave field. Analysis of (12) yields that the
phase of $R_{\alpha\alpha}$ does not depend on ζ if the wave field is symmetric i.e. $E_+ \equiv E_-$.
If there is a dominance of energy in one of the spectral components, say E_σ, then
the rate of change of the phase shift in $R_{\alpha\alpha}$ with separation is simply

$$\frac{d\tau}{d\zeta} = \frac{\partial R_{\alpha\alpha}/\partial\zeta}{\partial R_{\alpha\alpha}/\partial\tau} \simeq \frac{\sigma\beta}{\omega} = c_\sigma^{-1} \tag{14}$$

This relation allows one to determine the direction and magnitude of the vertical
phase propagation in the wave field. The pattern of phase shifts recognizable in
Fig. 10 is supported in a consistent way by all other combinations of instruments
not shown. The lag τ_m corresponding to the first maximum in the correlation
function has been plotted against the separation of the corresponding instru-
ments in Fig. 11. Since $d\tau/d\zeta>0$, there is a dominant upward phase propagation,
and hence a downward propagation of energy. The vertical phase speed $c_+ = 0.027$ cm/
sec estimated from Fig. 11 agrees with the findings of Perkins and Van Leer (1977)
from their repeated current profiling in the GATE area. The vertical wave length
$2\pi/\beta \simeq 2\pi c_+/f$ turns out to be about 75 m. In view of the vertical variations of
the stability frequency this order of magnitude of the vertical wavelength makes
the adequacy of WKB somewhat questionable. However, the results of our analysis
are correct to some degree since the large-scale waves do not feel the actual
$N(z)$-profile but rather a smoothed one. The effect of deviations may be treated
as a scattering problem of WKB waves on a smooth profile with variations in
$N(z)$ on a scale comparable to the wavelength (see e.g. Barcilon and others, 1972;
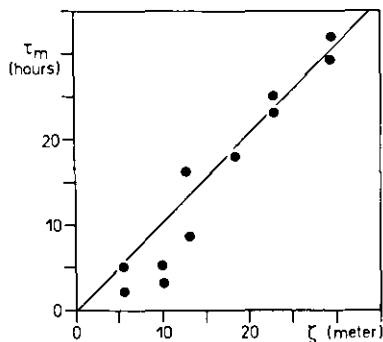Müller and Olbers, 1975).

Fig. 11. Lag τ_m of correlation maximum vs. vertical separation ζ
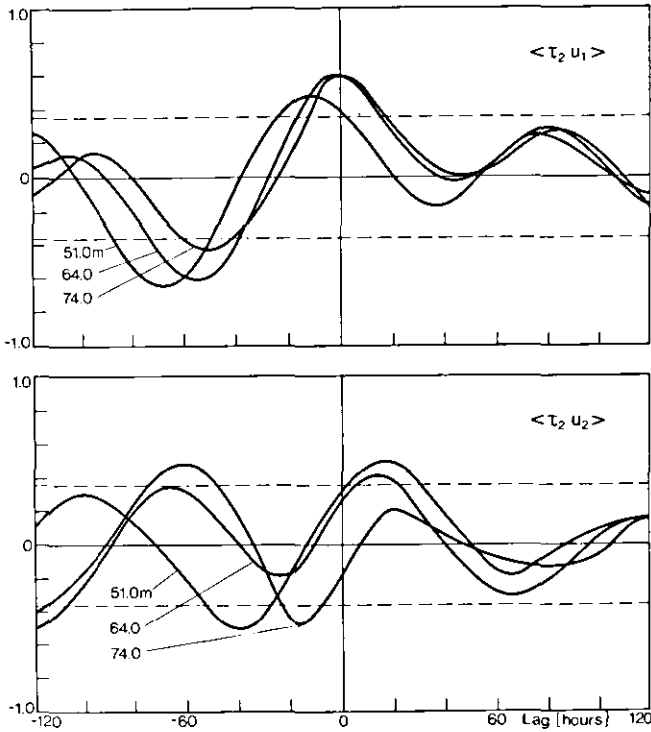for all correlation functions of same current components
in the thermocline.

Fig. 12. Correlation functions of eastward wind stress component τ_2 with the current u_α ($\alpha = 1, 2$) in the thermocline.

EVIDENCE FOR WIND-DRIVEN INTERNAL WAVES

Linear correspondences between the wind stress and the current in the mixed layer have been demonstrated above. Here we will search for a coupling of these fields with the wave field in the thermocline. A section of the correlation pattern across the base of the mixed layer is given in Figs. 12 and 13 which display some current-current correlations (c-c) and stress-current correlations (s-c). Correlations with the deepest instrument at 216 m depth (not shown) are insignificant, those above are significant at the 90 % confidence limits. In general, c-c correlations are larger than s-c correlations. Further, c-c correlations of east components and s-c correlations involving τ_2 are slightly larger than others (those involving τ_1 are not displayed). This is presumably due to larger variances in the time series of u_1 at instrument 12 and τ_2 (see Table 1). The dependence of the maximum correlation level on the separation is certainly not monotonic. In general there is a maximum correlation at

intermediate separations and a decrease to lower values at smaller and larger
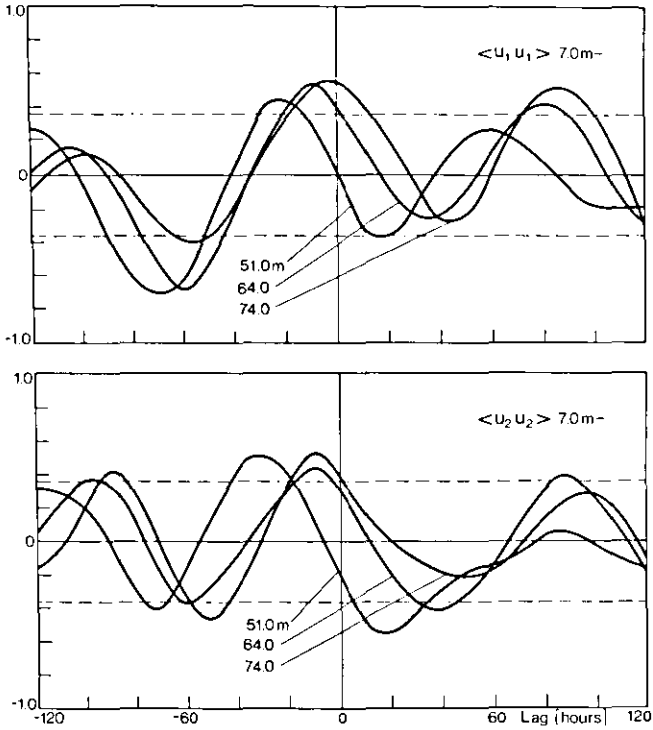separations.

Fig. 13. Correlation functions of same current components across
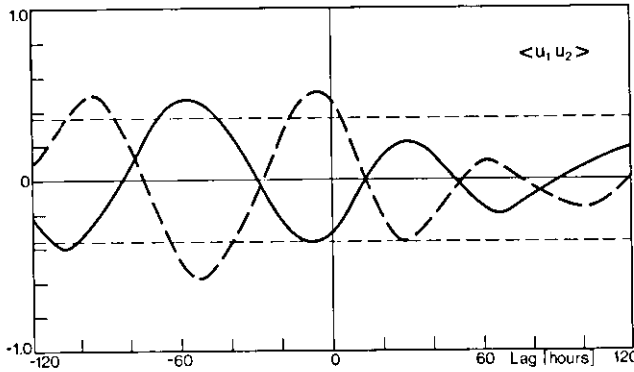the base of the mixed layer.

Fig. 14.Correlation functions of u_1 and u_2 across the base of the mixed layer.

Though some of the correlations are but marginally significant the overall appearance of the correlation pattern gives ample evidence of a wind-driven contribution to the motion in the thermocline. Further support can only be achieved by searching for consistencies with specific coupling models. Since the wave field is correlated with both, the wind stress and the inertial currents in the mixed layer, coupling of the waves to the wind stress via Ekman suction is likely. In addition to correlations this model implies simple phase relations between the wave field and the horizontal mass flux M_α in the mixed layer. From (7) we find

$$\begin{pmatrix} M_1 (\underset{\sim}{k},\omega) \\ M_2 (\underset{\sim}{k},\omega) \end{pmatrix} = \frac{i}{\omega^2 - f^2} \begin{pmatrix} \omega & -if \\ if & \omega \end{pmatrix} \begin{pmatrix} \tau_1 (\underset{\sim}{k},\omega) \\ \tau_2 (\underset{\sim}{k},\omega) \end{pmatrix} \tag{15}$$

According to the Ekman suction model internal waves are resonantly generated by the divergence of M_α. The amplitudes $a_+ (\underset{\sim}{k},\omega)$ of the downward propagating wave groups are then given by

$$a_+ (\underset{\sim}{k},\omega) = \frac{1}{\omega \psi_+ (-d)} \ k_\alpha \ M_\alpha (\underset{\sim}{k},\omega) \tag{16}$$

Inserting this into (8) we find that at near-inertial frequencies (where $M_1 \simeq iM_2$) the current of the wave field is approximately given by

$$u_\alpha = -\int d^2 k \int d\omega \ M_\alpha \ \frac{i\beta\psi_+(z)}{\psi_+(-d)} \ e^{i(\underset{\sim}{k}\cdot\underset{\sim}{x}-\omega t)} + c.c. \tag{17}$$

The absolute phase between M_α and u_β strongly depends on depth because of the almost discontinuous behaviour of the $N(z)$-profile in the upper part of the thermocline. However, the phase lag between M_1 and u_1 is the same as that between M_2 and u_2 whereas there is a phase difference of π between the pairs (M_1, u_2) and (M_2, u_1). Estimating the mass flux M_α by $d \cdot u_\alpha$ at 7 m presumably introduces only a small error in the phase. Correlations between the mixed layer current at 7 m depth and the current in the thermocline clearly show the above phase relations (Fig. 13 and 14). However, the consistency of this phase pattern with the Ekman suction model is a very weak statement since it is not independent of the approximate phase difference of $\pi/2$ between the current components at each depth discussed in the last section.

SUMMARY AND DISCUSSION

The following main results were obtained from our correlation analysis of a low-frequency current data set in the GATE area:

(a) The current system can be described by linear models.

(b) The mixed layer current is consistent with a linear model of wind-driven inertial oscillations.

(c) The current in the thermocline can be represented by a linear internal wave field of downward propagating wave groups.

(d) There is evidence of a linear coupling of the wave field to the wind stress. The coupling mechanism is consistent with an Ekman suction model.

The first three statements agree with previous work on inertial motions in the upper ocean. However, the existence of wind-driven internal waves has not yet been established. Earlier studies of inertial motions were mainly performed in mid- and high latitudes where there is a mismatch in the dominant time scales of the wind and the inertial period. Inertial motions are therefore mainly generated and destroyed by localized events in the wind field like storms and fronts. Intermittent occurrence of the oscillations in space and time are therefore a characteristic feature. Correspondences between wind and currents below the mixed layer can only be detected if the events are tracked along the rays. These, however, have extremely small slopes so that waves observed at some depth in the thermocline are related to the driving field some tens or even hundreds of kilometres away. The present type of experiments with emphasis on vertically spaced instruments and sparse horizontal coverage is in fact inadequate to search for a coupling of the internal wave field to the wind.

Approaching the equator the inertial period increases towards the time scale of synoptic disturbances in the atmosphere which have periods of 3 to 5 days. Hence inertial motions are resonantly generated by wind fluctuations. Local correspondences between wind and waves in the thermocline can be detected if the wind field has a large horizontal correlation scale. Even then correspondences may be masked by free wave components (or other 'noise') or by interaction processes affecting the forced wave components along the rays. The observed tendency of the wave field towards isotropy at greater depths may be an indication of nonlinear interactions within the wave field. The travel time of near-inertial waves (estimates of the vertical group velocity are given below) from the base of the mixed layer to our deeper instruments is about 2-5 periods which might be long enough for interactions to become effective (McComas, 1977).

Even if contaminations are disregarded the pattern of correlations between the wind stress and the wind-driven current field in the thermocline has a rather complex structure. General expressions for the cross-spectral matrix of a forcing field at the surface and the generated wave field are given in the appendix. Detailed comparison of the observed correlations with those of a linear forcing model is prohibited because sufficient knowledge about the horizontal structure of the wind stress field is lacking. However, we can illustrate some general features and discuss the scales involved. Coherence will be used because of analytical convenience.

Let us consider the coherence pattern generated by a wind stress field of simple geometry via Ekman suction. Let $\tau_1 \equiv o$ and let τ_2 be a superposition of Fourier components with meridional wave vectors, i.e. the coherence function $\gamma(r_2,\omega)$ of τ_2 is independent of r_1 and symmetric in r_2. This essentially one-dimensional model may serve as a rough approximation for wind stress in the GATE region. Using (15) and (16) the analysis in the appendix shows that the coherence between the current $u_\alpha(\underset{\sim}{x},z,t)$ and the wind stress $\tau_2(\underset{\sim}{x}-\underset{\sim}{r},t)$ can be expressed in terms of $\gamma(r_2,\omega)$ as

$$\gamma_{cs}(\underset{\sim}{r},z,\omega) = \frac{\left|\gamma'(r_2 - \Delta,\omega)\right|}{\left|\gamma''(o,\omega)\right|^{1/2}} \qquad (18)$$

where the dash denotes differentiation with respect to r_2 and $\Delta(z,\omega)$ given by (A5) is the horizontal distance between $\underset{\sim}{x}$ and the intersection with the surface of the ray passing through $(\underset{\sim}{x},z)$ (a schematic view is given in Fig. 15). The coherence between different current components has a similar form involving the second derivative of $\gamma(r_2,\omega)$. The coherences remain constant along a ray and vanish at the inertial frequency since in general $\gamma(r_2,\omega)$ and its derivatives tend to zero at infinite horizontal separations. As function of separation γ_{cs} reflects the derivative of the coherence and therefore shows in general a larger spatial variability. As a remarkable feature γ_{cs} vanishes at zero separations. The coherence with the local wind stress (i.e. $\underset{\sim}{r} = o$) attains its maxima at depths z where $\Delta(z,\omega)$ coincides with an inflexion point of $\gamma(r_2,\omega)$. Our data substantiate a nonmonotonic behaviour of γ_{cs} but otherwise are inadequate for further comparison. The horizontal distance

$$\Delta(z,\omega) \approx z \frac{N}{f} \left(2 \frac{\omega-f}{f}\right)^{-1/2} \qquad (19)$$

to the intersection of the ray with the sea surface is of the order 100 km for our deeper instruments which presumably is less than the meridional coherence scale of the wind stress. In passing we note that the maximum value of γ_{cs} is very roughly given by the ratio of the microscale $(-\gamma''(o,\omega))^{-1/2}$ of the wind stress and the width of its first derivative.

There are a few signatures in the data, apart from the correlation pattern, which support the hypothesis of wind-driven internal waves. First of all the energy of the currents in the thermocline is propagating downward. A second consistent feature is the preferred meridional propagation characteristic of the wave field which, because of resonant excitation, has been impressed by the wind field: synoptic disturbances have zonal wavelengths of a few 1000 km and meridional length scales of a few 100 km (Reed and others, 1977). Also, the observed energetics are roughly consistent with theoretical concepts. The vertical energy flux of the wave field is given by

$$F = \langle wp \rangle = \Sigma v_\sigma(\underset{\sim}{k},\omega) \, E_\sigma(\underset{\sim}{k},\omega,z) \qquad (20)$$

where $E_\sigma(\underset{\sim}{k},\omega,z)$ is the spectrum of the energy per unit volume and $v_\sigma(\underset{\sim}{k},\omega)$ is the vertical component of the group velocity. For near-inertial waves

$$v_\sigma \approx -2\frac{\omega-f}{f}c_\sigma \qquad (21)$$

Thus the determination of F requires knowledge of the frequency shift $\frac{\omega-f}{f}$ which is beyond the resolution of our data. If we believe that the range $0.05 - 0.2$ obtained at mid-latitudes is applicable also near the equator we obtain, from our estimate of the vertical phase, the range $3 \cdot 10^{-3} - 10^{-2}$ cm/sec for the magnitude of v_+. Assuming that all the observed energy $\frac{1}{2}\rho\langle u_\alpha u_\alpha\rangle$ is in downward propagating waves the vertical energy flux is downward and of magnitude $(0.2-0.6) \times 10^{-3}$ W/m^2, which agrees with previous estimates (Leaman, 1976; Perkins and Van Leer, 1977). A theoretical transfer of 10^{-3} W/m^2 sec to the first few internal wave modes by Ekman suction has been found by Käse (1979) using the observed wind stress spectrum and stratification at the F1-site. The WKB approximation yields a similar result. Using (15) and (16) the energy flux in the near-inertial frequency band becomes approximately

$$F \approx \int d^2k \int d\omega \frac{P_{--}(\underset{\sim}{k},\omega)}{v_+(\underset{\sim}{k},\omega)} \qquad (22)$$

where P_{--} is the clockwise rotary wind stress spectrum (shown in Fig. 2). The estimate of v_+ yields $F \approx (0.7-2.0) \times 10^{-3}$ W/m^2. Thus, the estimates of the energy flux from the kinematic definition (20) and the dynamic expression (22) agree with $\frac{\omega-f}{f}$ on the larger side of the observational range.

The wind during phase III of GATE was extremely low, at 10 m height it never exceeded 10 m/s at the F1-site. Nevertheless, the energy flux obtained here for the low-frequency internal wave band in the upper ocean is comparable to transfer rates of interaction processes affecting the deep-sea internal wave field (Müller and Olbers, 1975). Though observations unanimously show downward propagation of near-inertial energy in the main thermocline (Leaman and Sanford, 1975; Leaman, 1976; Müller and others, 1978) it still remains questionable whether the energy flux associated with wind-driven internal waves contributes directly with its total magnitude to the deep-sea inertial peak. The travel time to the main thermocline is extremely long (a few months in our case) so that exchange of energy with internal waves of higher frequency by nonlinear interactions is likely to occur.

ACKNOWLEDGEMENTS

REFERENCES

BARCILON, A., S. BLUMSACK, and J. LAU (1972). Reflection of internal gravity
  waves by small density variations. Journal of Geophysical Research, 2,
  104-107.

DADDIO, E., W.M.J. WISEMAN JR., and S.P. MURRAY (1978). Inertial currents over
  the inner shelf near 30° N. Journal of Physical Oceanography, 8,
  728-730.

DAY, C.G., and F. WEBSTER (1965). Some current measurements in the Sargasso
  Sea. Deep-Sea Research, 12, 805-814.

GONELLA, J. (1971). A local study of inertial oscillations in the upper layers
  of the ocean. Deep-Sea Research, 18, 775-788.

GONELLA, J. (1972). A rotary-component method for analysing meteorological and
  oceanographic vector time series. Deep-Sea Research, 19, 833-846.

HANNAN, E.J. (1960). Time series analysis, Methuen, London, pp. 152.

HASSELMANN, K. (1970). Wave-driven inertial oscillations. Geophysical Fluid
  Dynamics, 1, 463-502.

KÄSE, R.H. (1979). Calculations of the energy transfer by the wind to near-
  inertial internal waves. Deep-Sea Research, 26 A, 227-232.

KÄSE, R.H., and G. SIEDLER (1979). Internal wave kinematics in the upper
  tropical Atlantic. Deep-Sea Research, GATE Supplement I to Vol. 26,
  161-189.

KUNDU, P.K. (1976). An Analysis of Inertial Oscillations Observed Near
  Oregon Coast. Journal of Physical Oceanography, 6, 879-893.

LEAMAN, K.D., and T.B. SANFORD (1975). Vertical energy propagation of inertial
  waves: A vector spectral analysis of velocity profiles. Journal of Geo-
  physical Research, 80, 1975-1978.

LEAMAN, K.D. (1976). Observations on the Vertical Polarization and Energy Flux
  of Near-Inertial Waves. Journal of Physical Oceanography, 6, 894-908.

MCCOMAS, C.H. (1977). Equilibrium mechanisms within the oceanic internal wave
  field, Journal of Physical Oceanography, 7, 836-845.

MCPHEE, M.G. (1978). A simulation of inertial oscillation in drifting pack ice.
  Dynamics of Atmospheres and Oceans, 2, 107-122.

MOFJELD, H.O., and D. MAYER (1976). Formulas used to analyse wind-driven
  currents as first-order autoregressive processes. NOAA Technical Memorandum
  ERL PMEL-7, pp. 21 (Unpublished document).

MÜLLER, P., and D.J. OLBERS (1975). On the Dynamics of Internal Waves in the
  Deep Ocean. Journal of Geophysical Research, 80, (2), 3848-3860.

MÜLLER, P., D.J. OLBERS, and J. WILLEBRAND (1978). The IWEX Spectrum. Journal
  of Geophysical Research, 83, 479-500.

OLBERS, D.J. (1976). Nonlinear energy transfer and the energy balance of the internal wave field in the deep ocean. Journal of Fluid Mechanics, 74, part 2, 375-399.

PERKINS, H., and J. VAN LEER (1977). Simultaneous Current-Temperature Profiles in the Equatorial Counter Current. Journal of Physical Oceanography, 7, 264-271.

POLLARD, R.T., and R.C. MILLARD (1970). Comparison between observed and simulated wind-generated inertial oscillations. Deep-Sea Research, 17, 813-821.

REDELL, R.D. (1979). Winderzeugte Trägheitsbewegungen und Energiekorrelationen interner Wellen im tropischen Atlantik. Diplom Thesis. Kiel University, pp. 60.

REED, R.J., C.D. NORQUIST, and E.E. RECKER (1977). The Structure and Properties of African Disturbances as Observed During Phase III of GATE. Monthly Weather Review, 105, 317-333.

SCHOTT, F. (1971). Spatial structure of inertial-period motions in a two-layered sea, based on observations. Journal of Marine Research, 29, 85-102.

STERN, M.E. (1977). Interaction of inertial-gravity waves with the wind. Journal of Marine Research, 35, (3), 479-498.

WEBSTER, F. (1968). Observations of inertial-period motions in the deep sea. Review of Geophysics, 6, 473-490.

YAO, N.C., S. NESHYBA, and H. CHREW (1977). Rotary Cross-Bispectra and Energy Transfer Functions Between Non-Gausian Vector-Processes. II Winds and Currents off the Oregon Coast. Journal of Physical Oceanography, 7, 892-903.

APPENDIX

Cross-spectra of internal waves driven at the surface

We derive relations between the cross-spectra of the surface forcing function and that of the generated wave field. For linear coupling there is a linear relation

$$a_+(\underset{\sim}{k},\omega) = T_j(\underset{\sim}{k},\omega)\,\Phi_j(\underset{\sim}{k},\omega) \qquad\qquad (A\ 1)$$

between the amplitudes of the generated waves propagating downward and the driving fields Φ_j (i.e. the wind stress or any other field; the index j may include a continuous component such as the vertical coordinate z).
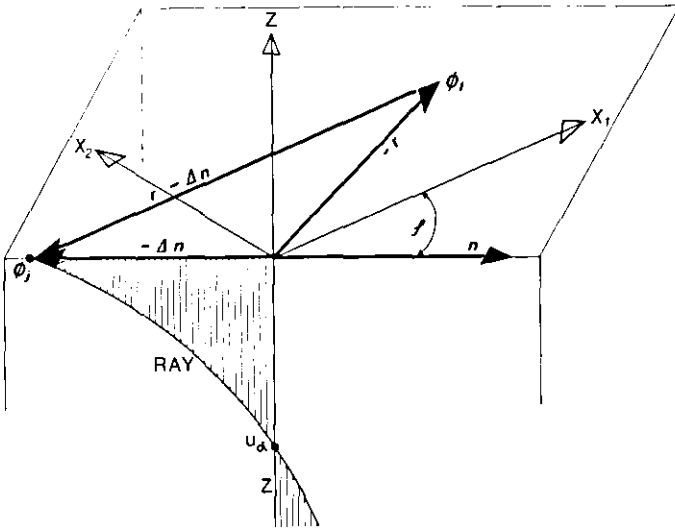

Fig. 15. Graph of the geometry associated with (A 3).

The cross-spectra of current components u_α and driving fields ϕ_ℓ may be expressed in terms of the cross-spectral matrix

$$\Gamma_{j\ell}(\underset{\sim}{r},\phi,\omega) = <\phi_j(\underset{\sim}{x},\phi,\omega)\phi_\ell^*(\underset{\sim}{x}-\underset{\sim}{r},\phi,\omega)> \tag{A 2}$$

$$= \int_0^\infty dk <\phi_j(k,\phi,\omega)\phi_\ell(k,\phi,\omega)> e^{ik(r_1\cos\phi + r_2\sin\phi)}$$

of the driving field components travelling in the ϕ-direction. Thus e.g.

$$A_{\alpha\ell}(\underset{\sim}{r},z,\omega) = <u_\alpha(\underset{\sim}{x},z,\omega)\phi_\ell^*(\underset{\sim}{x}-\underset{\sim}{r},\omega)>$$

$$= \int_0^{2\pi} d\phi\, U_\alpha(\phi,\omega)D_j(\phi,\omega)\Gamma_{j\ell}(r-\Delta\underset{\sim}{n},\phi,\omega) \tag{A 3}$$

where U_α is the eigen vector in the representation (8),

$$D_j(\phi,\omega) = T_j(-i\underset{\sim}{n} \cdot \underset{\sim}{\nabla},\phi,\omega) \tag{A 4}$$

with $\underset{\sim}{\nabla}=(\partial/\partial r_1,\partial/\partial r_2)$ and $n=(\cos\phi,\sin\phi)$ which is the unit vector in the ϕ-direction. Further

$$\Delta(z,\omega) = \int_z^{-d} d\zeta \left(\frac{N^2(\zeta)-\omega^2}{\omega^2-f^2}\right)^{1/2} \tag{A 5}$$

is the horizontal distance between the point $(\underset{\sim}{x},z)$ where the current u_α is observed and the intersection of the surface $z = -d$ of the ray passing through $(\underset{\sim}{x},z)$. The geometry associated with (A 3) is shown in Fig. 15. The representation (A 3) of $A_{\alpha\ell}$ illustrates a rather complex relation to the cross-spectra of the driving fields

$$C_{j\ell}(\underset{\sim}{r},\omega) = \int_0^{2\pi} d\phi\, \Gamma_{j\ell}(\underset{\sim}{r},\phi,\omega) \tag{A 6}$$

Here the contributions $\Gamma_{j\ell}$ from the different ϕ-directions are simply added whereas $A_{\alpha\ell}$ is superposition of directionally weighted derivatives of $\Gamma_{j\ell}$ sliding down the ray cone. A similar representation can be derived for the cross-spectral matrix of the current components

$$B_{\alpha\beta}(\underset{\sim}{r},z_1,z_2,\omega) = <u_\alpha(\underset{\sim}{x},z_1,\omega)u_\beta^*(\underset{\sim}{x}-\underset{\sim}{r},z_2,\omega)>$$

$$= \int_0^{2\pi} d\phi D_{\alpha\beta}\, D_j(\phi,\omega)D_\ell^*(\phi,\omega)\Gamma_{j\ell}(\underset{\sim}{r}-(\Delta_1-\Delta_2)\underset{\sim}{n},\phi,\omega) \tag{A 7}$$

Both cross-spectral matrices, $A_{\alpha\ell}$ and $B_{\alpha\beta}$ vanish at $\omega = f$ since here $\Delta \to \infty$ and generally $\Gamma_{j\ell}$ and its derivatives tend to zero at infinity. This reflects the fact that pure inertial oscillations generated at the surface do not penetrate into the thermocline.